Geopersia ***10*** *(2), 2020, PP. 289-303* *DOI: 10.22059/GEOPE.2019.291757.648510*

Facies analysis, petrography and geochemistry of the Neogene gypsum deposits in the Eshtehard area, Alborz Province, Iran

Masoomeh Zaheri, Behrouz Rafiei*
Department of Geology, College of Sciences, Bu–Ali Sina University, Hamedan, Iran
**Corresponding author, e–mail: b_rafiei@basu.ac.ir*
(*received: 01/11/2019 ; accepted: 28/12/2019*)

Abstract

The evaporite deposits examined in this study are located in the Eshtehard area (SW of the Alborz Province). Four outcrop sections (Mard Abad, Eshtehard, Salt Mine and Rud Shur) and thirty gypsum samples were selected for facies analysis, petrographical and mineralogical investigation in combination with the geochemical analyses. The Neogene evaporites are composed of massive, selenite, nodular and satin–spar gypsum lithofacies. Three different textures were recognized under microscope: porphyroblastic, alabastrine, and fibrous gypsum. Petrographical investigations and X–ray diffraction analysis showed the evaporite beds are mainly composed of gypsum, with no anhydrite relics. The characteristics of these litho– and microfacies indicate gypsum deposited in the lacustrine and sabkha settings. The ICP–OES analysis shows significant differences in major and trace element contents of the four types of gypsums. The concentrations of Sr, Fe, Al, Mg and Na were increased in massive gypsum, while the crystals represent a decreased in size. The contents of these elements were also decreased in nodular, fibrous and selenite gypsums. These are probably indicating an increase and decrease in brine concentration, respectively. Paleoclimate condition is simply determined for the Neogene evaporites using geochemical approach. The results suggest a shift from semi–arid (bottom) to arid (top) paleoclimate conditions.

Keywords: *Gypsum Texture, Lacustrine Environment, Strontium, Neogene Deposits, Eshtehard, Alborz Province*

Introduction

Non–marine evaporite deposits are common features of arid closed basins. Most modern non–marine evaporites and almost all ancient non–marine evaporites occur in saline lacustrine settings (*e.g.,* Strakhov, 1970; Hardie *et al*., 1978; Lu, 2000; Warren, 2007). The term saline lacustrine is sometimes referred to as perennial/ephemeral lake, playa–lake, salt pan, and inland sabkha (Nichols, 2009). The most comprehensive overviews on the sedimentology of non–marine evaporites have been considered by Strakhov (1970), Glennie (1970, 1987), Cooke & Warren (1973), Eugster & Hardie (1975), Hardie *et al*., (1978), Attia *et al*. (1995), Lu (2000), and Warren (2007, 2016).

Evaporite minerals are important indicators for the paleodepositional environments and paleoclimate because they reflect the hydrogeochemical conditions at the time of their precipitation (Yang *et al*., 2014; Playa *et al*., 2007; Smykatz–Kloss & Roy, 2010; Li *et al*., 2010, 2013; Bahadori *et al*., 2011; Dill *et al*., 2012; Tangestani & Validabadi, 2014).

Gypsum ($CaSO_4.2H_2O$) is one of the most abundant calcium sulfate mineral precipitated when the salinity of solution increases to about five times of the modern seawater salinity and give information regarding the brines from which they precipitate (Warren, 1999). Primary gypsum is directly precipitated from brine, and the original textures are preserved. Therefore, primary gypsum is characterized by the absence of solid inclusions of precursor anhydrite (relics) (Ingerson, 1968; Holliday, 1970; Dronkert, 1985; Warren, 1999). Diagenetic gypsum is also precipitated from fluids of dissolved evaporates and it does not represent morphologies inherited from precursor anhydrite (Ortí & Rosell, 2000).

Major and trace elements can be incorporated into gypsum by the following processes (McIntire, 1963): 1) substitution for Ca^{2+} in the $CaSO_4$ lattice, 2) surface adsorption, 3) non–sulfate solid inclusions (such as carbonate, salt, or clay), and 4) defects in minerals. Therefore, they can affect the gypsum morphology and crystal size (Edinger, 1973; Ichikuni & Musha, 1978; Kushnir, 1980; McCaffrey *et al*., 1987; Franchini–Angela & Rinaudo, 1989; Guan *et al*., 2010; Rossi *et al*., 2011; Otalora & Garcia–Ruiz, 2014). These behaviors form a basis for utilizing element concentrations as geochemical indicators to decipher the paleosalinity of the depositional environment (Kushnir, 1980, 1981; Ullman & McLeod, 1986; Lu *et al*., 1997, 2002).

Gypsum deposited have outcropped in the Central Iran and Zagros zones. The Neogene (Miocene–Pliocene) evaporites such as the Upper Red Formation (in the Central Iran zone) exposed in the north, center, and east of Iran, comprising 73.2% of

the total gypsum outcrops in Iran (Raeisi *et al*., 2013). In the study area, gypsum deposits are also observed in the units M_1 and M_3 with a relatively considerable thickness (Fig. 2). The investigation on these evaporates can be an important contribution for a better understanding of the paleoenvironment, paleoclimate, and paleosalinity of the Neogene red deposits (units M_1 and M_3) in the northwest of Central Iran zone. The purposes of this study are: 1) to interpret gypsum facies and depositional environment, 2) identification and interpretation of gypsum textures, and 3) the influence of geochemistry on the crystal morphology and size.

Geographical and Geological setting

The Eshtehard area is located in the northwest of Central Iran and south of Central Alborz structural zones, adjacent to the Urumieh– Dokhtar magmatic belt (Fig. 1A). The Neogene red deposits covers an area about 120 km^2 along the northern margin of Eshtehard city (35°, 45', 00 to 35°, 50', 00 N and 50°, 10', 00 to 50°, 55', 00 E) in the southeast of Karaj (Alborz Province) (Fig. 1B). The Eocene magmatic rocks are also seen in the south of the Eshtehard area. The Neogene deposits unconformably overlie the Eocene volcanic rocks in the southern part of the study area. The Eocene volcanic rocks are composed of basalt to andesite, and green to cream tuffs with the andesitic, dacitic, and rhyolitic composition (Mahdizadeh, 1995; Yousefi, 2000) (Fig. 1C).

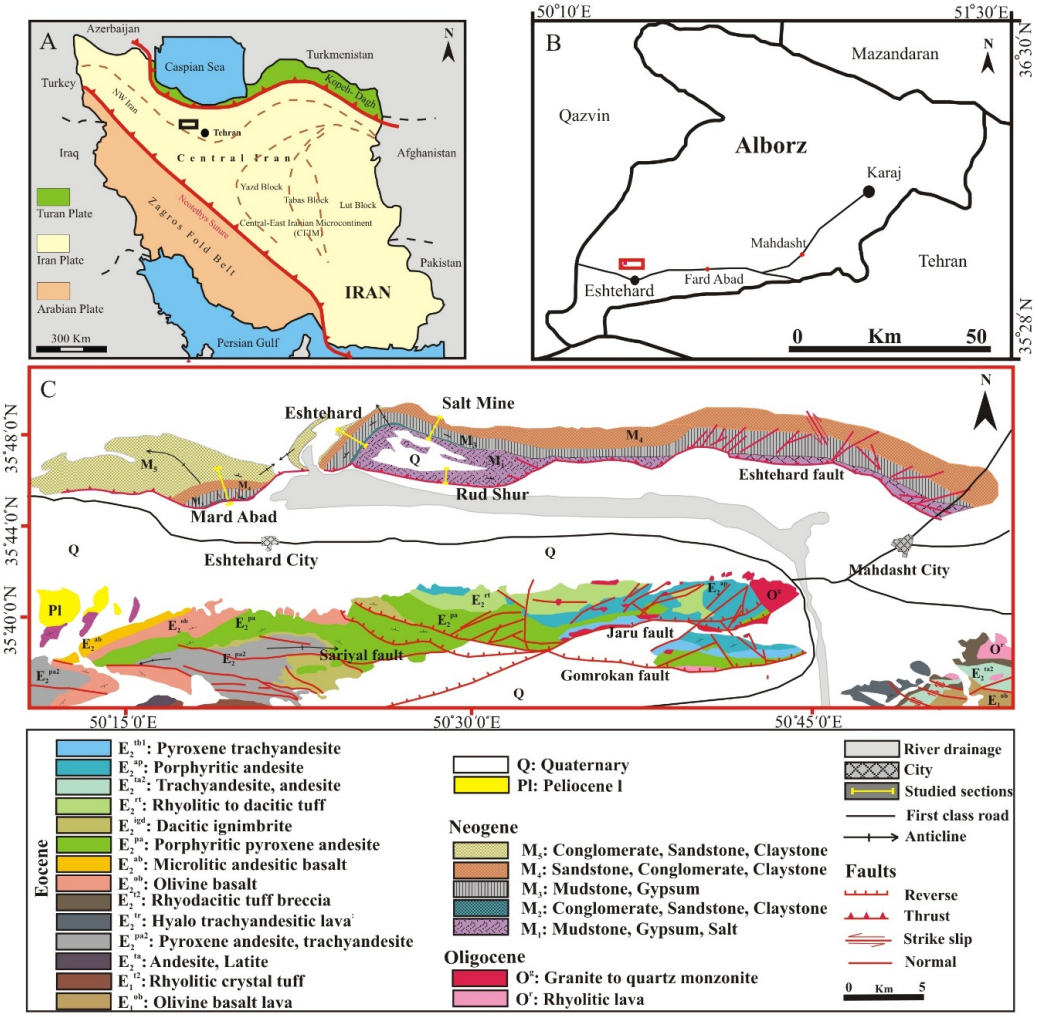

Figure 1. Locality map of the study area and measured stratigraphic sections in the NW of Central Iran zone. A) present-day map of Iran with the structural zones (modified from Wilmsen *et al*., 2009), B) geographical location. The study area is marked with a red rectangle), and C) simplified geological map of the Eshtehard area with the location of the four measured sections (Mahdizadeh, 1995 & Yousefi, 2000).

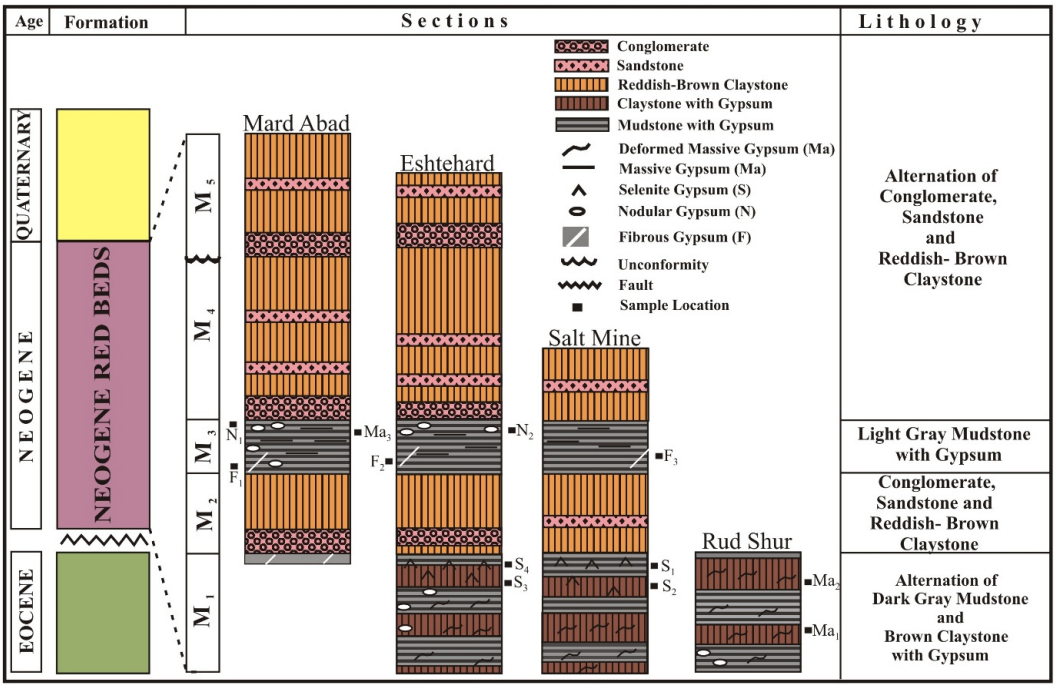

Figure 2. Simplified lithostratigraphic columns of the Neogene successions in the four study sections (thickness not to scale) with five distinct lithology units (M_1 to M_5) (The location of each section is shown in Fig. 1C).

The Neogene red beds in the study area were investigated in four outcrops, including Mard Abad (1080 m in thickness), Eshtehard (820 m), Salt Mine (550 m), and Rud Shur (300 m) sections (Fig. 1C). The studied Neogene successions consist of gypsiferous brown claystone/gray mudstones and sandstone/conglomerate intercalated with reddish–brown claystone deposits (Fig. 2). Therefore, according to their lithofacies changes, the Neogene successions have been subdivided into the five units (M_1 to M_5). The units M_1 and M_3 consist of an alternation of gypsiferous dark brown claystone/gray mudstone, and gypsiferous light gray mudstone, respectively, while units M_2, M_4 and M_5 are characterized by conglomerate/ sandstone bodies intercalated with reddish–brown claystone deposits (Fig. 2).

Materials and Methods

Detailed field investigations were carried out on the Neogene evaporite units (M_1 and M_3) of the Eshtehard area. A total of forty–five gypsum samples were selected from the four sections. Fourteen representative thin sections were prepared for petrographic studies. Cutting, polishing, and thinning processes were performed using an oil system in the Geological Department of the Kharazmi University, Tehran, Iran. All of the thin sections were then examined using a polarizing microscope. The crystal fabrics and texture types of gypsum minerals were mainly described, according to Ortí *et al*., (2010) and Warren (2016).

Bulk gypsum samples were grounded using an agate mortar to <74 µm for mineralogical composition and geochemistry analyses. The mineralogical analysis was performed on the powdered bulk samples (Four samples) using an Italstructures diffractometer with Cu kα radiation. The diffractometer was operated at 30 mA, 40 kV, from 2–60˚2Θ, at Bu–Ali Sina University, Hamedan, Iran. Twelve gypsums facies, with different crystal morphologies (massive, nodular, selenite and satin– spar) were analyzed for their Sr, Al, Fe, Mg, Na, Li, and Ti contents using ICP–OES (varian 735) in the Zarazma, Mineral Studies Company, Tehran, Iran.

Results and discussion

Gypsum lithofacies and depositional environment

Gypsum lithofacies are only observed in the units M_1 and M_3, which are intercalated with detrital brown claystone and gray mudstones. Unit M_1 is mainly characterized by the high thickness of deformed massive, and selenite gypsums, while unit M_3 is composed of layered massive, nodular and satin spar gypsums (Fig. 2).

Massive gypsum facies

This facies is generally observed in the units M_1 and M_3 in the four measured sections (Fig. 2) and constitutes more than 40% of the four gypsum facies. The thickness of an individual bed of the white to dark–colored massive gypsum varies from 5 to 10 centimeters. They extend laterally up to several hundred meters, and are found interbedded with dark brown claystone and gray laminated mudstones. This lithofacies often displays a regular alternation of massive gypsum and claystone/mudstones facies, and suggests a "gypsum–claystone/mudstone rhythmical pattern" (Fig. 3 A, B). The presence of fine–grained deposits partings between the massive gypsum beds testifies to the cyclical flooding of the evaporite basin by undersaturated continental waters (*e.g.,* Bertini, 2006; Stefano *et al*., 2010). The massive gypsum horizons frequently display folding (micro and macro folds) in the unit M_1 in the Rud Shur section (Fig. 3A). These structures may be developed due to tectonic movements occurring during or post–deposition (Arenas & Pardo, 1999; Testa & Lugli, 2000).

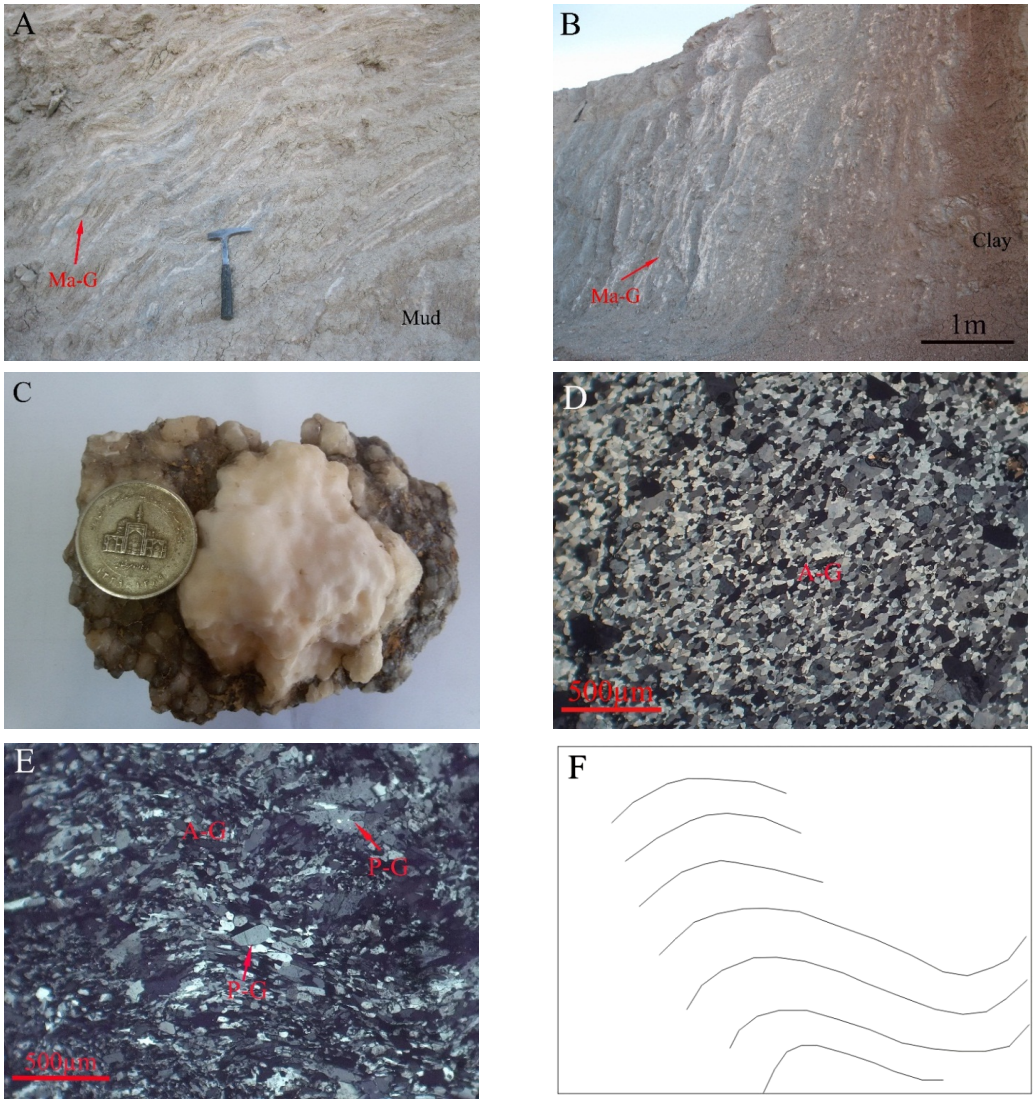

Figure 3. Field photos and microscopic characteristics of the massive gypsum facies from the unit M_1 in the Rud Shur section; A, B) field photograph of massive gypsum with macro folds, intercalated within claystone, and mudstone, C) the hand specimen of massive gypsum with black impurities (Coin diameter is about 2.5 cm), D) fine-grained alabastrine gypsum that contains anhedral features showing crystals ~100 µm in size, E) dynamic texture with fine- and coarse- ameboid crystalline gypsum, F) schematic image from dynamic texture. (Ma-G: massive gypsum, A-G: alabastrine gypsum, P-G: porphyroblastic gypsum, Mud: mudstone, Clay: claystone).

In some cases, the presence of black discoloration or impurities (clay, manganese oxide, mafic rock fragments) in this gypsum type may be due to the mixing during primary sedimentary processes, or be present as the result of the secondary effects such as solution, weathering, and erosion (Mason & Moore, 1982) (Fig. 3C).

Petrographical studies showed alabastrine texture is the main existing texture found in the massive gypsum lithofacies. The alabastrine texture is a general term, and sometimes referred to microcrystalline gypsum due to the nature of microcrystal aggregations (*e.g.,* Testa & Lugli, 2000). We used the terms of alabastrine and porphyroblastic textures following by Holliday (1970). In this study, alabastrine gypsum occurs in limpid and fine–grained crystals from 50 to 100 µm in size. This texture containing xenotopic to idiotopic crystals, were formed by fine–grained equidimensional gypsum crystals in addition to coarse–crystalline anhedral texture. The xenotopic texture indicates a mosaic of anhedral crystals with poorly defined to sutured crystal boundaries, which have irregular or undulatory extinction (Fig. 3D). Besides alabastrine texture, the dynamic texture was also observed in massive gypsum microfacies. This texture is observed in the unit M_1 of the Rud Shur section, where layers are folded (Figs. 2 and 3 A, B). This dynamic gypsum includes cloudy ameboid crystals, medium in size (up to 200µm), irregular crystal boundaries, undulose optical extinction, and aligned–flowing texture (Fig. 3E, F). Massive gypsum microfacies is characterized by the absence of anhydrite relics. It is believed that this facies was deposited originally under subaqueous conditions in a saline lacustrine environment (*e.g.,* Schreiber *et al*., 1976; Warren, 1999, 2006).

Selenite gypsum facies

This facies was observed in the upper part of unit M_1 in the Salt Mine, Eshtehard, and Mard Abad sections (Fig. 2) and includes about 25% of the total gypsum facies. The translucent or red–colored selenite gypsums are represented by crystals with 4–15 cm in height and 2–5 cm in width, which exhibits twins, meanwhile the twin plane oriented upwards. This lithofacies in the uppermost of the unit M_1 in Salt Mine area is intercalated with the brown claystone and gray mudstone (Fig. 4A, B).

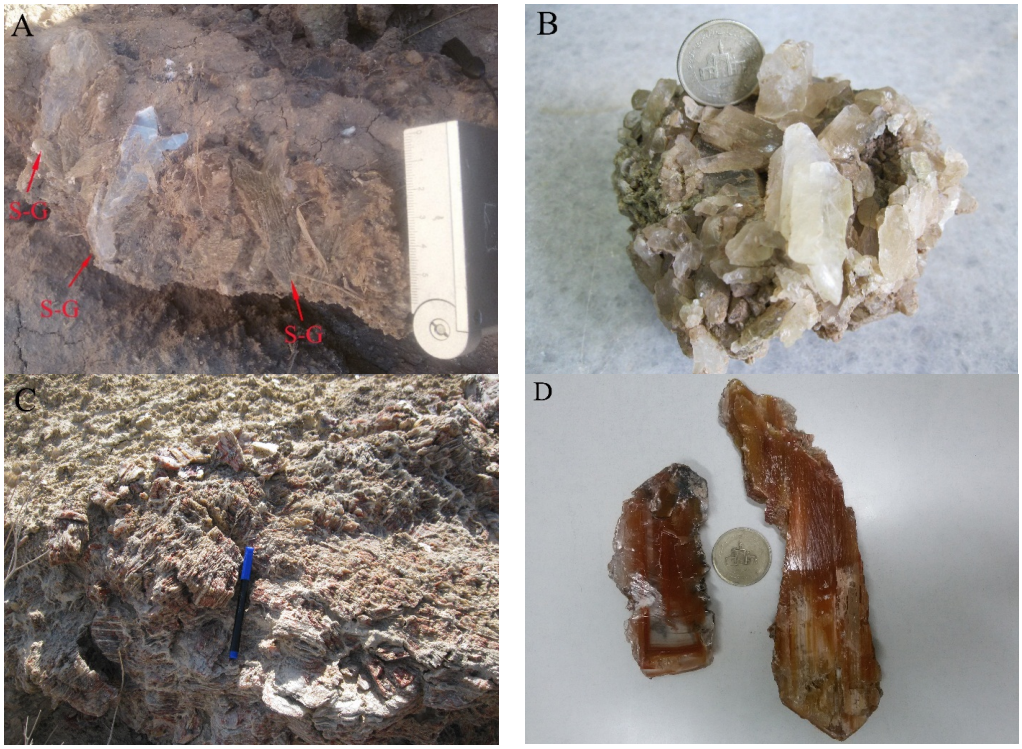

Figure 4. Field photos of selenite gypsum facies from the unit M_1; A) close up view of selenite (swallowtail) crystals intercalated within brown claystone, the Salt Mine section, B) the hand specimen of translucent selenite gypsum (the length crystals between 1 – 5 cm) (Coin diameter: 2.5 cm), C) field photo from red- colored massive selenite gypsum (7-15 cm in height and 2-5 cm in width), in the Eshtehard section, (Pen length: 15 cm), D) red-colored selenite gypsum crystals in hand specimen (coin diameter: 2.5 cm).

Red–colored massive selenite gypsum beds with selenite crystals up to 15 cm in length were also observed in the middle part of unit M_1 in the Eshtehard section (Fig. 4C, D). The continuous growth of large selenite crystals represents the maximum water level with progressive increasing of the salinity which causes the growth of the large crystals (Babel, 2004). When high salinity condition was longer–lasting, thick bodies of massive selenite gypsum were formed (Peryt, 2001). The continuous growth of large crystals may also suggest a low degree of supersaturation. Low saturation of the brines is typical for growing large crystals (Babel, 1999a). These exclusive characteristics of the two cycles are important for stratigraphic correlation and reconstruction of paleodepth and salinity (Babel, 2004). Red discoloration results from mud staining and the presence of iron oxides impurities (Abrantes *et al*., 2016). Therefore, massive selenite facies in the middle part of unit M_1 indicates deposition occurred in a relatively deep setting, while individual selenite gypsum in the uppermost of unit M_1 is attributed to a shallower depositional environment (tens of centimeters to few meters) and gypsum precipitation was mainly occurred under stable salinity conditions (Warren, 2006).

Nodular gypsum facies

This lithofacies is present in some places of the units M_1 and M_3 in the Eshtehard, Mard Abad, and Rud Shur sections (Fig. 2). Nodular gypsum facies consists of around 25–30% of the total gypsum lithofacies. Individual pale yellow to white–colored gypsum nodules are elliptical or spherical and ranges between 5– 17 cm in size (Fig. 5 A). Banded nodular gypsum consists of closely packed and elongated masses parallel to bedding planes, which passes laterally and vertically into claystone or mudstone. Layers of flattened nodules have 0.5 to 1 m thickness, and lateral continuity varies from 15–120 m, which are completely separated from each other by thin mudstone films (Fig. 5 B). The formation of nodular structures is probably result of water table fluctuations and evaporation processes inside sediments at the margin of saline lacustrine or sabkha environments in an arid to semi–arid climate (*e.g.,* Mossop & Shearman, 1973; Kendall, 1981; Warren, 1999, 2006).

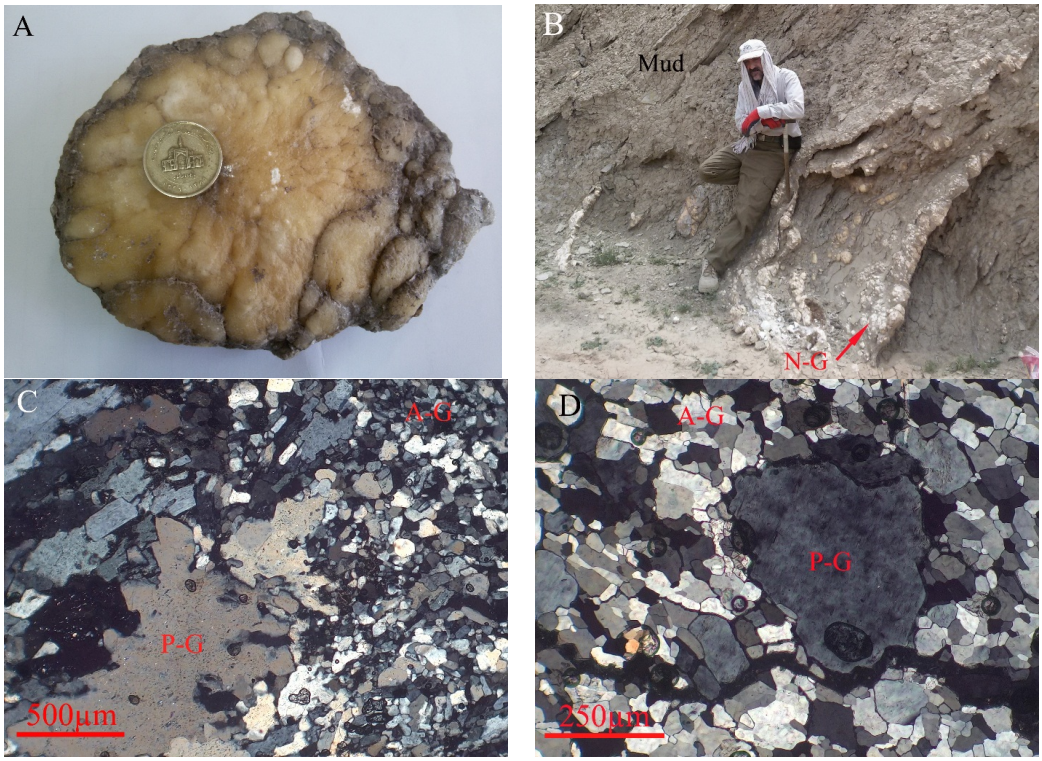

Figure 5. Field and microscopic photographs from the nodular gypsum facies in unit M_3; A) nodular gypsum in hand specimen (coin diameter: 2.5 cm), B) banded nodular gypsum facies interbedded with gray mudstone and brown claystone, C, D) porphyroblastic texture of nodular gypsums. Note that these anhedral to subhedral porphyroblasts (up to 2 cm in length) have no anhydrite relics. (N-G: nodular gypsum, A-G: alabastrine gypsum, P-G: porphyroblastic gypsum).

Petrographically, nodular gypsum indicates porphyroblastic texture associated with the alabastrine texture. This is composed of very limpid, typically with no inclusion, fine to coarse anhedral to subhedral crystals (crystal size between <10µm to >100µm) and planar to interlocking crystal boundaries, which showing sharp extinction. Porphyroblasts occur as individual or in groups of two or three crystals surrounded by fine or alabastrine gypsum crystals (Fig. 5 C, D). This microfacies is also characterized by the absence of anhydrite relics similar to massive gypsum microfacies.

Therefore, the nodules formed in units M_1 and M_3 are primary gypsum with no evidence of the hydration of anhydrite to gypsum.

Satin spar (fibrous) gypsum facies

This lithofacies was observed in the limited parts of unit M_3 at the Mard Abad and Eshtehard sections, and is composed of about 10% of the total gypsum lithofacies (Fig. 2). Additionally, satin spar gypsum is intercalated within brown claystone and gray mudstone deposits similar to those of gypsum lithofacies (Fig. 6A). Satin spar gypsum is used as a general term for the needle–shaped gypsum crystals infilling veins and fractures and is widespread in the mudstone and shales adjacent to bedded evaporite units undergoing dissolution (*e.g.,* Shearman *et al*., 1972; El–Tabakh *et al*., 1998; Warren, 2006, 2016).

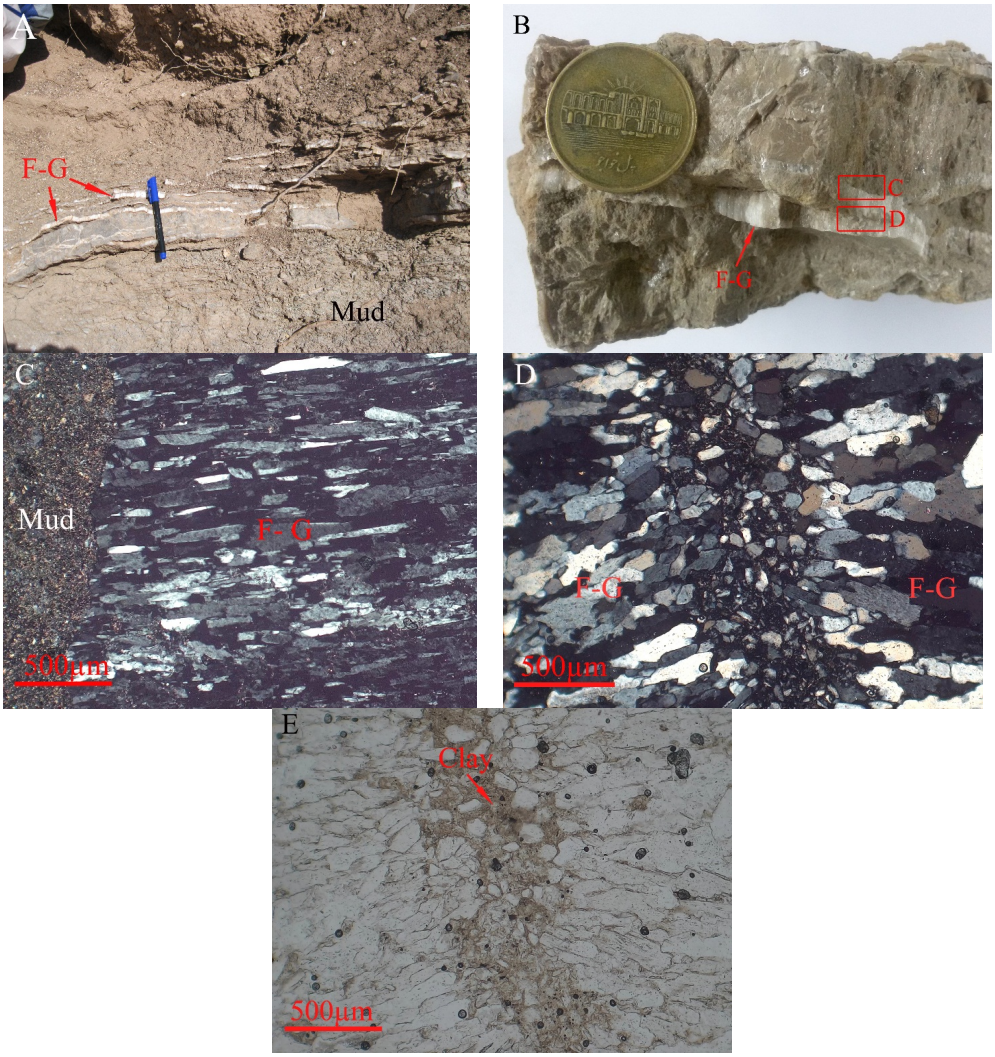

Figure 6. Field photo and microscopic characteristics of the fibrous (satin spar) gypsum facies from unit M_3, A) field photograph of fibrous gypsum facies intercalated within gray mudstone, (Pen length: 15 cm), B) fibrous gypsum (1 cm in thickness) in hand specimen, (Coin diameter: 2.5 cm), C) microphotographs of fibrous gypsum in contact with mudstone, D) and E) clay concentration at the boundary between fibrous gypsum (F-G), D- XPL. (F-G: fibrous gypsum, Mud: mudstone).

In this study, the thickness of satin– spar or fibrous gypsum layers vary from 0.5 to 3 cm, and the crystals are oriented at a steep angle or perpendicular to the vein walls (Fig. 6A, B). Undersaturated fluids with respect to sulfate minerals move along fractures, dissolve the gypsum and, or anhydrite (releasing Ca^{2+} SO_4^{2-}), and then after the supersaturation, they are deposited as gypsum mineral. This process occurs via dissolution–precipitation with an increase in volume (Holliday, 1970; Shearman, 1985). They suggest the final stage of evaporite formation, during the uplift of sediments in the telogenes phase (Holliday, 1970; Shearman *et al*., 1972; Warren, 2006; Abrantes *et al*., 2016).

Petrographical studies on fibrous (satin spar) gypsum lithofacies show subhedral to anhedral crystals >200 μm in length with sharp extinction. The large crystals of fibrous gypsum have grown perpendicular on the mudstone walls (Fig. 6C). The filling of fractures is marked by anhydrite–free gypsum crystals that decrease in size from the edge (about 0.6mm) to the center (around 0.2mm) (Fig. 6D), usually with the long axes perpendicular to the fracture walls. Locally, detrital clay mineral or rarely carbonate cement developed as filling porosity in fibrous gypsum (Fig. 6D, E). Many authors consider satin spar gypsum as a by–product of the rehydration process of anhydrite (*e.g.* Shearman *et al*., 1972; Testa & Lugli, 2000), but no anhydrite relicts were found in fibrous samples (Fig. 6C, D). Satin spar morphology also reflects crystal growth from very pure, supersaturated fluids, which favored extreme elongation parallel to the c–axis (Magee, 1991).

The investigated Neogene evaporites were deposited originally as gypsum under saline lacustrine conditions. Gypsum types intercalated within brown claystone and gray mudstone indicate a shallow lacustrine or playa depositional setting (*e.g.,* Mossop & Shearman, 1973; Kendall, 1981; Warren, 1999, 2006). Many ancient saline playas, documented in the literatures, were developed in arid and semi–arid climates (Clemmensen, 1979; Yang *et al*., 1995; Playa *et al*., 2007; Li *et al*., 2010, 2013; Smykatz–Kloss & Roy, 2010; Bahadori *et al*., 2011; Dill *et al*., 2012; Tangestani & Validabadi, 2014). Evaporites are formed under arid climatic conditions where total evaporation exceeds the net inflow of solute–bearing waters and are an indicator of ancient arid climates (Hardie, 1984). Therefore, this would suggest that the climate condition in the Eshtehard area was arid to semi–arid during the Neogene. This observation represents an important contribution for a better understanding of the Neogene climate in the northwest of the Central Iran zone.

The bulk mineralogy of evaporite samples

X–ray diffraction investigation reported from representative gypsum samples in this study reveal that the Neogene evaporites are primarily composed of gypsum with no anhydrite relict (Fig. 7A). The results of XRD analyses of massive gypsum with impurities mainly represents gypsum as main mineral phases as well as minor amount of illite, quartz and calcite (Fig. 7B). Gypsum was identified by diffraction peaks at 11.62, 20.70, 23.37 and 29.09 2θ.

Geochemistry

Element distribution

Cations such as Sr^{2+}, K^{+}, Na^{+}, Mg^{2+} and Fe^{+} as well as some impurities may be incorporated into gypsum lattice via substitution for Ca^{2+} (similar ionic radii) during the co–precipitation process. It is also proposed that Sr^{2+}, Mg^{2+}, and K^{+} concentrations in gypsum depend upon three factors including growth rate, temperature and their concentrations in brine (Kushnir, 1980; Guan *et al*., 2010; Rossi *et al*., 2011; Otalora & Garcia–Ruiz, 2014).

Brine concentration probably plays an important role versus Sr^{2+}, K^{+}, Mg^{2+} and Mn^{2+} contents in gypsum under the various depositional environments. As brine concentration increases, the amounts of Sr^{2+}, K^{+}, Mg^{2+} and Mn^{2+} also increase and relatively more strontium, potassium, magnesium and manganese will be incorporated into the growing crystals and their inhibitory effect increases on the growth rate of gypsum crystals (Edinger, 1973; Kushnir, 1980; Franchini–Angela & Rinaudo, 1989; Guan *et al*., 2010; Rossi *et al*., 2011; Otalora & Garcia–Ruiz, 2014).

Examined gypsum samples for trace element contents include three massive, two nodular, four selenite, and three fibrous (satin spar) that were selected from the four study sections (Figs. 1C, and 2). Elements concentrations within the four types of gypsum (massive, nodular, selenite and fibrous) are given in Table 1. It is known that the massive samples with impurities generally show higher element values than the nodular, selenite, and satin–spar gypsum samples (Table 1).

Table 1. Concentration of major and minor elements (in ppm) for the four gypsum types in the study areas.

	Sr	Fe	K	Na	Al	Ti	Mg	Li	Mn	Na/K	Na_2O/Al_2O_3	Na_2O/Fe_2O_3
DL	0.5	100	100	100	100	10	100	1	5	-	-	-
***Ma$_1$**	1364	9450	4994	3331	16397	1070	4548	10	168	0.66	0.14	0.33
***Ma$_2$**	1024	2102	1089	719	3097	172	1233	3	42	0.66	0.16	0.33
***Ma$_3$**	592	158	110	390	203	22	<100	1	6	3.54	1.25	2.5
Mean	993.33	3903.33	2064.33	1480.00	5665.66	421.33	-	5	72.00	1.62	0.51	1.05
N_1	843	<100	<100	362	<100	14	<100	1	<5	-	-	-
N_2	890	112	<100	422	140	15	<100	1	<5	-	2.00	3
Mean	866.50	-	-	392.00	-	14.50	-	1	-	-	-	-
F_1	203	110	<100	371	122	17	<100	1	<5	-	2.5	2.5
F_2	207	<100	<100	354	<100	13	<100	<1	<5	-	-	-
F_3	357	861	<100	364	<100	14	<100	1	<5	-	-	0.41
Mean	255.66	-	-	363.00	-	14.66	-	1	-	-	-	1.45
S_1	200	104	<100	366	130	16	<100	1	<5	-	2.5	5
S_2	259	157	129	362	232	19	<100	1	8	2.8	1.25	2.5
S_3	156	<100	<100	314	<100	93	<100	1	6	-	-	-
***S_4**	299	1002	790	504	1707	12	581	1	35	0.63	0.2	0.5
Mean	228.50	-	-	386.50	-	35.00	-	1	-	1.71	1.31	2.66

* Along with impurities

Ma: Massive gypsum, N: Nodular gypsum, S: Selenite gypsum, F: Fibrous gypsum, DL: Detection Limit, -: not detectable.

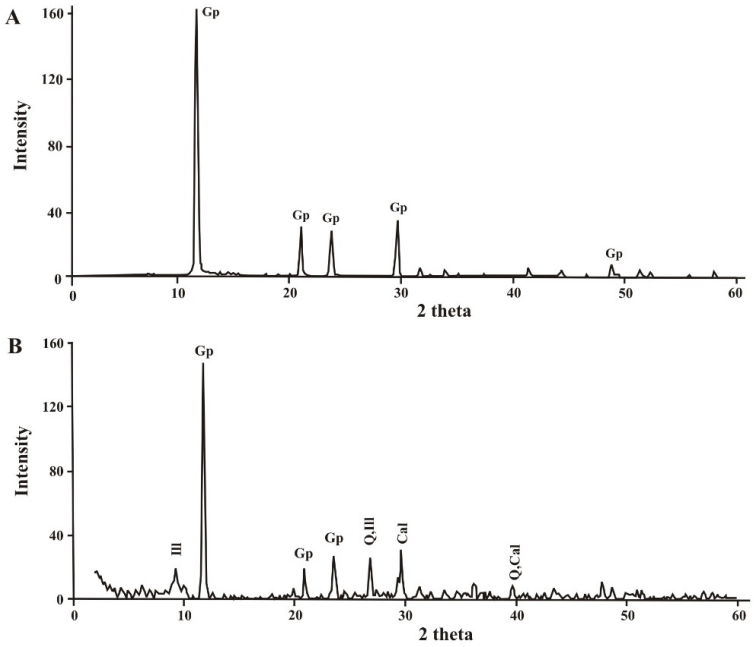

Figure 7. X-ray diffraction patterns from representative bulk samples, A) nodular gypsum, no anhydrite content, from unit M_3, in the Mard Abad section, B) massive gypsum with mud impurities (sample Ma_1) from unit M_1, in the Rud Shur section. (Gp: gypsum, Ill: Illite, Q: Quartz: Cal: Calcite).

The mean of strontium in the massive, nodular, selenite and fibrous samples is 960.00, 866.50, 255.66 and 228.50 ppm, respectively. Massive gypsum samples contain high amount of strontium than nodular, selenite, and fibrous gypsum (Table 1). The mean concentrations of Fe, K, Al, Ti and Li in the massive gypsum samples are 3903.33, 2064.33, 5665.66, 421.33 and 5 ppm, respectively, which are very high compared to other gypsum samples (Table. 1) (Fig. 8A). The high concentration of mentioned elements in massive gypsums can be attributed to the presence of detrital materials and clay impurities (Figs. 3C and 7B), iron oxide, and other compounds (Tumuklu, 2016). Both iron and titanium are hydrolysates elements and so they accumulate in fine–grained sediments (Mason &

Moore, 1982; Smykatz–Kloss *et al*., 1998, 2004).

High K and Al contents in the massive gypsum compared with the other gypsum samples are due to the presence of illite as impurities. Also, relatively high Li concentration in massive gypsum (Ma_1 and Ma_2) (Table. 1) is attributed to the presence of the detrital particles or clay minerals, similar to K and Al contents (Smykatz–Kloss *et al*., 1998, 2004).

The Na/K ratio was determined for the studied gypsum samples. This ratio is high in the selenitic gypsums (except sample S_4) and low in massive gypsums with clay impurities (samples Ma_1 and Ma_2) (Table 1). The concentration of K^+ in the pure gypsum is less than that of Na^+. Adsorption of K^+ on the active surfaces of clay and detrital minerals may account for the absence of this element in the lacustrine or marine brine concentration (Averty & Paytan, 2003).

The Na_2O/Al_2O_3 and Na_2O/Fe_2O_3 ratios from evaporite minerals are used as indicators of paleoclimatic conditions in arid regions. These ratios strongly increase with increasing aridity (or decreasing water activity) and decrease with decreasing aridity (or increasing water activity) conditions (Smykatz–Kloss & Roy, 2010). Nesbitt and Young (1982) were pioneers in the use of such ratios for palaeoclimatic determination. Different authors also continued in characterising palaeoclimatic conditions by using of these ratios (Sirocko, 1995; Gallet *et al*., 1996; Smykatz–Kloss *et al*., 1998, 2004; Rögner *et al*., 2004; Schütt, 2004; Roy *et al*., 2008, 2009; Sinha *et al*,. 2006).

In the studied samples, nodular (N_2), fibrous (F_1), selenite (S_1, S_2, and S_3), and massive (Ma_3) gypsums showed strong increasing of these ratios, while massive (Ma_1 and Ma_2) and selenite (S_4) gypsums indicated a significant decreasing in these ratios. Decreasing in the Ma_1, Ma_2 and S_4 samples can be attributed to the lower aridity than the other gypsums, during their precipitations (Fig. 8B).

Strontium geochemistry and gypsum morphology

Different crystal morphologies occur during the precipitation of gypsum. There are many factors affecting gypsum crystal morphology, such as nucleation and growth rates, additional ions, organic matter, saturation state, pH, groundwater depth (Edinger, 1973; Liu & Nancollas, 1973; Cody, 1979; Last & Schweyen, 1985; Cody & Cody, 1988; Magee, 1991; Bosbach & Hochella, 1996; Hamdona & Hadad, 2008; Guan *et al*., 2010; Mees *et al*., 2012).

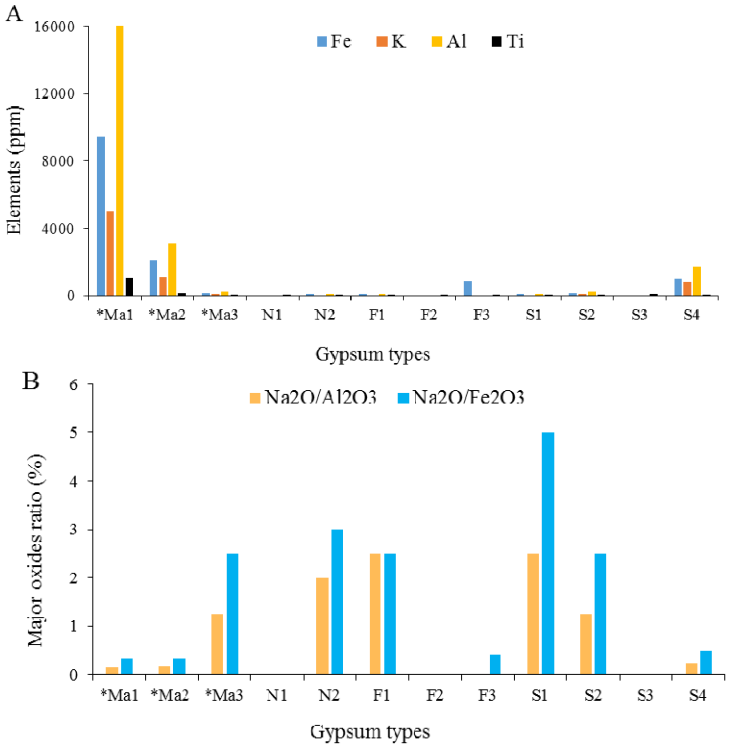

Figure 8. A) Elements concentration (ppm) versus gypsum types, and B) major oxides ratio (%) versus gypsum types (Data from Table. 1), (Ma: Massive, N: Nodular, S: Selenite, F: Fibrous).

Of these factors, the growth rate of crystals is important. When, gypsum precipitated from brines exhibits a high growth rate, crystal size is small (Edinger, 1973; Cody & Cody, 1988; Zhang & Nancollas, 1992). Rosell *et al*., (1998) mentioned that salinity, temperature, brine concentration, crystal size, and growth rate are the main factors governing Sr co–precipitation with gypsum.

Based on gypsum lithofacies, macroscopic and microscopic analyses, four gypsum types with different morphologies (massive, Nodular, satin–spar and selenite) and textures (alabastrine and porphyroblastic) were identified in the study sections (units M_1 and M_3). They exhibit small and large crystal sizes, respectively (Figs. 3–6).

The difference in Sr concentration within the four gypsum types (Table. 1) is a function of its concentration in the original brine, where they were precipitated (Rosell, 1998). In this study, the mean strontium concentration progressively decreases from massive (960.00), nodular (866.50), and fibrous (255.66) to selenite (228.50) gypsums (Table. 1) (Fig. 9A). This difference is due to the different modes of precipitation of each type (Aljubouri, 2011).

A higher strontium concentration in massive gypsum indicates higher degree of supersaturation or higher growth rate, resulting in smaller crystal size. On the other hand, lower strontium concentration in selenite gypsum, indicates lower degree of supersaturation, which leads to a slower growth rate and resulting in relatively large crystal size (Zhang & Nancollas, 1992; Aljubouri, 2011).

In the studied samples, the average crystal sizes of massive, nodular, satin– spar and selenite gypsums are 0.15, 10, 15, and 75 mm, respectively (Table. 2).

The relationship between the gypsum type, crystal size, and strontium content is shown in Table 2. The negative correlation between crystal size and strontium concentration was first reported by Butler (1973) for Sr in gypsum samples from Abu Dhabi and confirmed by Kushnir (1980), for Sr in gypsum samples from Bardawil sabkha in northern Sinai. In the present study, this negative relationship is clearly shown in Fig. 9 A, B. The logarithmic plot gives a negative trend with the following equation (Aljubouri, 2011):

$$\text{Log } Y = -0.298 * \log \text{size } (X) + 3.668 \qquad \text{Eq. 1}$$

Where (Y) represents the concentration of Sr in gypsum. Using this equation, it is possible to calculate strontium concentration for any of the four gypsum types.

Therefore, the high Sr^{2+} content can be attributed to co–precipitation with the massive and nodular gypsums, in this study. Moreover, this premise is supported by the results of microscopic studies (fine crystalline or alabastrine texture) (Figs. 3D, E and 5C, D).

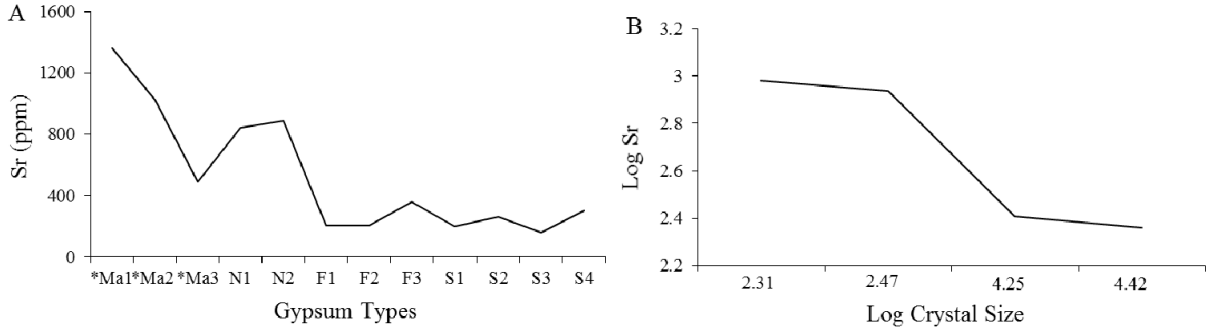

Figure 9. Bivariate-plots of A) Sr versus Gypsum types (Data from Table 1) and B) Log Sr versus Log crystal size (Data from Table. 2). Note to negative correlations between Sr concentration and gypsum types / crystal size, (Ma: Massive, N: Nodular, S: Selenite, F: Fibrous).

Table 2. Relationship between average crystal size and strontium concentration.

Type of gypsum	Average Crystal Size (mm)	Average Sr (ppm)	Log Crystal Size	Log Sr
Massive	0.15	960.00	2.31	2.98
Nodular	10	866.50	2.47	2.93
Fibrous	50	255.66	4.25	2.40
Selenite	75	228.50	4.42	2.35

The enrichment may be due to an additional Sr coming from the dissolution of early gypsum, or from supply via a synsedimentary influx of water (Tekin, 2001). The concentration of Sr in solution is low (limited by the solubility of $SrSO_4$) and the number of Sr ions coprecipitating with gypsum is comparable with the number of Sr ions in the brine. Thus the concentration of Sr in the brine changes considerably as more gypsum crystallizes (Sonnenfeld, 1984; Tekin, 2001).

Sources of gypsum

Determination of gypsum source whether in bed–rock and surface or underground water, is essential (Watson, 1985). The investigations of Khalili *et al*. (2007) on the evaporitic deposits (D member) of the Qom Formation in the Central Iran zone, represent that the sulfur in the evaporitic deposits (D–member) was very likely derived from the oxidation of pyrite, chalcopyrite and calcium–rich minerals present in the magmatic rocks. In the study area, gypsum does not exist in the bedrocks (Fig. 1C). The bed rocks of the study area are predominantly Eocene andesite to andesitic basalt and they are devoid of gypsum. The sulfur in the Neogene evaporitic deposits (units M_1 and M_3) was likely derived from the old evaporitic deposits such as the Qom Formation located in the western part of the study area (Qazvin and Avaj–Abegarm area).

Conclusions

The Neogene deposits at the Eshtehard area unconformably overlie the Eocene basement rocks and subdivided into five units (M_1 to M_5). Evaporitic successions (M_1 and M_3) consist of several kinds of gypsum facies, such as massive, nodular, selenite and satin spar (fibrous). Three different gypsum textures were determined as alabastrine, porphyroblastic and fibrous. The facies identified in the units M_1 and M_3 were interpreted as shallow lacustrine environments (massive and selenite gypsum) to the playa or in inland sabkha (nodular gypsum) environments, under an arid to semi–arid climate with seasonal water level changes.

The microscopic and XRD investigations reported in present study, reveal that the Neogene evaporites are primarily composed of micro– to course–crystalline gypsum without anhydrite relict.

Geochemistry analyses reveal that the high concentration of Sr, Al, Fe, K, Na, Ti, Mg and Li in the massive gypsum rather than nodular, fibrous and selenite gypsum mainly depend on high growth rate, detrital impurities and brine concentration. The negative correlation between gypsum crystal size and strontium concentration in the gypsum types represents the inhibitory effect of strontium on the growth rate of crystals.

The Na_2O/Al_2O_3 and Na_2O/Fe_2O_3 ratios from gypsum samples in the lower and middle parts of unit M_1 (massive gypsum) indicate low aridity paleoclimate conditions, while the upper part of unit M_1 (selenite gypsum) and unit M_3 (nodular and fibrous gypsums) represent high aridity paleoclimate conditions.

Acknowledgments

We acknowledge the research council of Bu–Ali Sina University for the financial support.

References

Abrantes, F.R., Nogueira, A.C.R., Soares, J.L., 2016. Permian paleogeography of west–central Pangea: Reconstruction using sabkha–type gypsum–bearing deposits of Parnaíba Basin, Northern Brazil, Sedimentary Geology, 341: 175–188.

Aljubouri, Z. A., 2011. Geochemistry of calcium sulphate rocks of Fat`ha Formation at four localities within Nineveh District, Northern Iraq (with emphasis on strontium distribution), Iraqi National Journal of Earth Sciences, 11: 49–70.

Arenas, C., Pardo, G., 1999. Latest oligocene–late miocene lacustrine systems of the north–central part of the Ebro Basin (Spain): Sedimentary facies model and palaeogeographic synthesis, Palaeogeography, Palaeoclimatology, Palaeoecology: 151: 127–148.

Attia, O.E., Lowenstein, T.K., Wali, A.M.A., 1995. Middle Miocene gypsum, Gulf of Suez: marine or nonmarine? Journal of Sedimentary Research: 65: 614–626.

Averty, K.B., Paytan, A., 2003. Empirical partition coefficients for Sr and Ca in marine barite: implications for reconstructing seawater Sr and Ca concentrations. Geochemistry, Geophysics, Geosystems, 4: 1525–2027.

Babel, M., 1999a. Facies and depositional environments of the Nida Gypsum deposits (Middle Miocene, Carpathian Foredeep, southern Poland). Geological Quarterly, 43: 405−428.

Babel, M., 2004a. Models for evaporite, selenite and gypsum microbialite deposition in ancient saline basins. Acta Geologica Polonica, 54: 219–249.

Bahadori, A., Carranza, E.J.M., Soleimani, B., 2011. Geochemical analysis of evaporite sedimentation in the Gachsaran Formation, Zeloi oil field, southwest Iran. Journal of Geochemical Exploration, 111: 97–112.

Bertini, A., 2006. The Northern Apennines palynological record as a contribute for the reconstruction of the Messinian palaeoenvironments. Sedimentary Geology, 188: 235–258.

Bosbach, D., Hochella, M.F., 1996. Gypsum growth in the presence of growth inhibitors: a scanning force microscopy study. Chemical Geology. 132: 227–236.

Butler, G.P., 1973. Strontium geochemistry of modern and ancient calcium sulphate minerals. In The Persian Gulf, Springer, 423–452.

Clemmensen, L.B., 1979. Triassic lacustrine red–beds and paleoclimate: The "Buntsandstein" of Helgoland and the Malmros Klint Member of East Greenland. Geologische Rundschau. 68: 748–774.

Cody, R.D., 1979. Lenticular gypsum: occurrences in nature, and experimental determinations of effects of soluble green plant material on its formation. Journal of Sedimentary Research, 49: 1015–1028.

Cody, R.D., Cody, A.M., 1988. Gypsum nucleation and crystal morphology in analog saline terrestrial environments. Journal of Sedimentary Research, 58: 247–255.

Cooke, R. U., and Warren, A., 1973. Geomorphology in Deserts. Univ. of Calif. Press, Los Angcles, 374 pp.

Dill, H.G., Bechtel, A., Berner, Z., Botz, R., Kus, J., Heunisch, C., Hamad, A.M.B.A., 2012. The evaporate–coal transition: chemical, mineralogical and organic composition of the Late Triassic Abu Ruweis Formation, NW Jordandreference type of the "Arabian Keuper". Chemical Geology, 299: 20–40.

Dronkert, H., 1985. Evaporite models and sedimentology of Messinian and Recent evaporites. GUA Papers of Geology, 24: 1–283.

Eugster, H.P., Hardie, L.A., 1975. Sedimentation in an ancient playa–lake complex: the Wilkins Peak Member of the Green River Formation of Wyoming. Geological Society of America Bulletin, 86: 319–334.

Edinger, S.E., 1973. An investigation of the factors which affect the size and growth rates of the habit faces of gypsum. Journal of Crystal Growth, 18: 217–224.

El–Tabakh, M., Schreiber, B.C., Warren, J.K., 1998. Late fibrous fracture–fill within non–marine strata of the Newark Rift Basin, Eastern North America. Journal of Sedimentary Research, 68: 88–99.

Franchini–Angela, M., Rinaudo, C., 1989. Influence of sodium and magnesium on the growth–morphology of gypsum, $CaSO_4.2H_2O$. Neues Jahrbuch Fur Mineralogie–Abhandlungen, 160: 105–115.

Gallet, S., Jahn, B.M., Torii, M., 1996. Geochemical characterization of the Luochuan loess–paleosol sequence, China, and paleoclimatic implications: Chemical Geology, 133: 67–88.

Glennie, K.W., 1970. Desert sedimentary Envirmments. Elsevier Publ. Co., New York, 222 pp.

Glennie, K.W., 1987. Desert sedimentary environments, present and past – a summary. Sedimentary Geology, 50: 135–165.

Guan, B., Yang, L., Wu, Z., 2010. Effect of Mg^{2+} ions on the nucleation kinetics of calcium sulfate in concentrated calcium chloride solutions. Industrial & Engineering Chemistry Research, 49: 5569–5574.

Hamdona, S.K., Hadad, O.A.A., 2008. Influence of additives on the precipitation of gypsum in sodium chloride solutions. Desalination, 228: 277–286.

Hardie, LA., 1984. Evaporites: Marine or non–marine? American Journal of Science, 284: 193–240.

Hardie, L.A., Smoot, J.P., Evgster, H.P., 1978. Saline lakes and their deposits: A sedimentological approach. Modern and Ancient Lake Sediments, International Association of Sedimentologists, 7–41.

Holliday, D.W., 1970. The petrology of secondary gypsum rocks. Journal of Sedimentary Research, 40: 734–744.

Ichikuni, M., Musha, S., 1978. Partition of strontium between gypsum and solution. Chemical Geology, 21: 359 363.

Ingerson, E., 1968. Deposition and geochemistry work sessions. In: Mattox RB, *et al*. (ed.) Saline Deposits, New York: The Geological Society of America. Special Paper, 88: 671–681.

Kendall, A.C., 1981. Continental and supratidal (Sabkha) evaporates. In: Walker, R.G. (Ed.), Facies Models. Geoscience Canada, 1: 145–157.

Kushnir, J., 1980. The coprecipitation of strontium, magnesium, sodium, potassium, and chloride ions with gypsum, an experimental study. Geochimica et Cosmochimica Acta, 44: 1471–1482.

Kushnir, J., 1981. Formation and early diagenesis of varved evaporite sediments in a coastal hypersaline pool. Journal of Sedimentary Research 51, 1193–1203.

Last, W.M., Schweyen, T.H., 1985. Late Holocene history of Waldsea Lake, Saskatchewan, Canada. Quaternary Research, 24: 219–234.

Li, M., Fang, X., Wang, J., Song, Y., Yang, Y., Zhang, W., Liu, X., 2013. Evaporite minerals of the lower 538.5 m sediments in a long core from the Western Qaidam Basin, Tibet. Quaternary International, 298: 123–133.

Li, M., Fang, X., Yi, C., Gao, S., Zhang, W., Galy, A., 2010. Evaporite minerals and geochemistry of the upper 400m sediments in a core from the Western Qaidam Basin, Tibet. Quaternary International, 218: 176–189.

Liu, S.T., Nancollas, G.H., 1973. The crystal growth of calcium sulfate dihydrate in the presence of additives. Journal of Colloid and Interface Science, 44: 422 429.

Lu, F.H., 2000. Sedimentology and geochemistry of late Miocene carbonates and evaporites, Nijar Basin, southeastern

Spain. Unpublished Ph. D dissertation, SUNY, Stony Brook., 198 pp.
Lu, F.H., Meyers, W.J., Hanson, G.N., 2002. Trace elements and environmental significance of Messinian gypsum deposits, the Nijar Basin, southeastern Spain. Chemical Geology, 192: 149–161.
Lu, F.H., Meyers, W.J., Schoonen, M.A.A., 1997. Minor and trace element analyses on gypsum: an experimental study, Chemical Geology, 142: 1–10.
Mahdizadeh, S., 1995. Geologic Map of Karaj, Geological Survey of Iran, Tehran, scale 1:100000.
Magee, J.W., 1991. Late Quaternary lacustrine, groundwater, aeolian and pedogenic gypsum in the Prungle Lakes, southeastern Australia. Palaeogeography, Palaeoclimatology, Palaeoecology, 84: 3–42.
Mason, B., Moore, C.B., 1982. Principles of Geochemistry: New York, Wiley, 344 pp.
McIntire, W.L., 1963. Trace element partition coefficients e a review of theory and applications to geology. Geochimica–Cosmochimica Acta, 27: 1209–1264.
McCaffrey, M.A., Lazar, B., Holland, H.D., 1987. The evaporation path of seawater and the co–precipitation of Br^- and K^+ with halite. Journal of Sedimentary Research, 57: 928–937.
Mees, F., Casteneda, C., Herrero, J., Ranst, E.V., 2012. The nature and significance of variations in gypsum crystal morphology in dry lake basins. Journal of Sedimentary Research, 82: 37–52.
Mossop, G.D., Shearman, D.J., 1973. Origins of secondary gypsum rocks. Trans. Inst. Min. Metall, 82: 147–154.
Nesbitt, H.W., Young, G.M., 1982. Early Proterozoic climates and plate motions inferred from major element chemistry of lutites. Nature, 299: 715–717.
Nichols, G., 2009, Sedimentology and Stratigraphy, 2nd ed. Wiley–Blackwell, 419 pp.
Ortí, F., Rosell, L., 2000. Evaporative systems and diagenetic patterns in the Calatayud Basin (Miocene, central Spain). Sedimentology, 47: 665–685.
Ortí, F., Rosell, L., Anadón, P., 2010. Diagenetic gypsum related to sulfur deposits in evaporates (Libros Gypsum, Miocene, NE Spain). Sedimentary Geology, 228: 304–318.
Otalora, F., Garcia–Ruiz, J., 2014. Nucleation and growth of the Naica giant gypsum crystals. Chemical Society Reviews, 43: 2013– 2026.
Peryt, T.M., 2001.Gypsumfacies transitions in basin–marginal evaporites: middle miocene (Badenian) of west Ukranie. Sedimentology, 48, 1103–1119.
Playa, E., Cendon, D.I., Trave, A., Chivas, A.R., García, A., 2007. Non–marine evaporates with both inherited marine and continental signatures: the Gulf of Carpentaria, Australia, at ~70 ka. Sedimentary Geology, 201: 267–285.
Raeisi, E., Zare, M., Aghdam, J.A., 2013. Hydrogeology of gypsum formations in Iran. Journal of Cave and Karst Studies, 75: 68−80.
Rögner, K., Knabe, K., Roscher, B., Smykatz–Kloss, W., Zöller, L., 2004. Alluvial loess in the Central Sinai: Occurrence, origin, and palaeoclimatological consideration, in Smykatz–Kloss, W., Felix–Henningsen, P. (eds.), Palaeoecology of Quaternary Drylands, Lecture Notes on Earth Sciences: Berlin, Springer, 79–99.
Rosell, L., Ortí, F., Kasprzyk, A., Playà, E., Peryt, T.M., 1998. Strontium geochemistry of Miocene primary gypsum: Messinian of Southeastern Spain and Sicily and Badenian of Poland. Journal of Sedimentary Research, 68: 63–79.
Rossi, M., Ghiara, M.R., Chita, G., Capitelli, F., 2011. Crystal–chemical and structural characterization of fluorapatites in ejecta from Somma–Vesuvius volcanic complex. American Mineralogist, 96: 1828–1837.
Roy, P.D., Caballero, M., Lozano, R., Smykatz–Kloss, W., 2008a. Geochemistry of late quaternary sediments from Tecocomulco Lake, central Mexico: Implication to chemical weathering and provenance: Chemie der Erde – Geochemistry, 68: 383–393.
Roy, P.D., Smykatz–Kloss, W., Morton, O., 2008b. Geochemical zones and reconstruction of late Holocene environments from shallow core sediments of the Pachapadra paleo–lake, Thar Desert, India: Chemie der Erde – Geochemistry, 68: 313–322.
Schreiber, B.C., Friedman, G.M., Decima, A., Schreiber, E., 1976. Depositional environments of Upper Miocene (Messinian) evaporite deposits of the Sicilian Basin. Sedimentology, 23: 729–760.
Schütt, B., 2004. The chemistry of playa–lake sediments as a tool for the reconstruction of Holocene environmental conditions – a case study from the central Ebro basin, in Smykatz–Kloss, W., Felix–Henningsen, P. (eds.), Palaeoecology of Quaternary Drylands, 5–30.
Shearman, D.J., 1985. Syndepositional and late diagenetic alteration of primary gypsum to anhydrite. In: Schreiber, B.C., Harner, H.L., (Eds.), Sixth International Symposium on Salt, Salt Institute, 1: 41–50.
Shearman, D.J., Mossop, G.D., Dunsmore, H., Martin, M., 1972. Origin of gypsum veins by hydraulic fracture. Trans. Inst. Min. Metall, 81: 149–155.
Sinha, R., Smykatz–Kloss, W., Stüben, D., Harrison, S.P., Berner, Z,. Kramar, U., 2006. Late Quaternary palaeoclimatic reconstruction from the lacustrine sediments of the Sambhar playa core, Thar Desert margin, India: Palaeogeography, Palaeoclimatology, Palaeoecology, 233: 252–270.

Sirocko, F., 1995. Abrupt change in monsoonal climate: evidence from the geochemical composition of Arabian Sea sediments: Kiel, University of Kiel, Habilitation thesis.

Smykatz–Kloss, W., Knabe, K., Zöller, L., Rögner, K., Hüttl, C., 1998. Paleoclimatic changes in Central Sinai, Egypt: Paleoecology of Africa, 25: 143–155.

Smykatz–Kloss, W., Smykatz–Kloss, B., Naguib, N., Zöller, L., 2004. The reconstruction of palaeoclimatological changes from mineralogical and geochemical compositions of loess and alluvial loess profiles, in Smykatz–Kloss, W., Felix–Henningsen, P. (eds.), Palaeoecology of Quaternary drylands, Lecture Notes on Earth Sciences: Berlin, Springer, 101–118.

Smykatz–Kloss, W., Roy, P.D., 2010. Evaporite mineralogy and major element geochemistry as tools for palaeoclimatic investigations in arid regions: a syn–thesis. Boletín de la Sociedad Geologica Mexicana, 62: 379 390.

Sonnenfeld, P., 1984. Brines and Evaporites. Academic Press, Orlando.

Stefano, L., Vinicio, M., Marco, R., Charlotte, S.B., 2010. The primary lower gypsum in the Mediterranean: A new facies interpretation for the first stage of the Messinian salinity crisis, Palaeogeography, Palaeoclimatology, Palaeoecology, 297: 83–99.

Tangestani, M.H., Validabadi, K., 2014. Mineralogy and geochemistry of alteration induced by hydrocarbon seepage in an evaporite formation; a case study from the Zagros Fold Belt, SW Iran. Applied Geochemistry, 41: 189–195.

Tekin, E., 2001. Stratigraphy, geochemistry and depositional environment of the celestine–bearing gypsiferous formations of the Tertiary Ulaş–Sivas Basin, East–Central Anatolia (Turkey). Turkish Journal of Earth Sciences, 10: 35–49.

Testa, G., Lugli, S., 2000. Gypsum–anhydrite transformations in Messinian evaporites of central Tuscany (Italy). Sedimentary Geology, 130: 249–268.

Tunuklu, A., Ciflikli, M., Ozgur, F.Z., 2016. Determination of the trace elements effecting on the color of the gypsum mineral, International Journal of Engineering Research and Management (IJERM), 3: 16–19.

Ullman, W.J., McLeod, L.C., 1986. The late–quaternary salinity record of lake Frome South Australia: evidence from Na^+ in stratigraphically–preserved gypsum. Palaeogeography, palaeoclimatology, palaeoecology, 54: 153–169.

Warren, J. K., 1999. Evaporites: Their evolution and economics. Oxford, UK, Blackwell Scientific, 438 pp.

Warren, J. K., 2007. Evaporites: Sediments, Resources and Hydrocarbons. Berlin, Springer, 1041 pp.

Warren, J. K., 2016. Evaporites: A Geological Compendium. London, Springer, 1822 pp.

Watson, A., 1985. Structure, chemistry and origins of gypsum crusts in southern Tunisia and the central Namib Desert. Sedimentology, 32: 855–875.

Wilmsen, M., Fürsich, F.T., Seyed–Emami, K., Majidifard, M.R., 2009a. An overview of the stratigraphy and facies development of the Jurassic System on the Tabas Block, east–central Iran, In: Brunet, M.–F., Wilmsen, M., Granath, J.W. (Eds.), South Caspian to Central Iran Basins. Geological Society of London, Special Publication, 312: 323–343.

Yang, Y., Fang, X., Galy, A., Li, M., Appel, E., Liu, X., 2014. Paleoclimatic significance of rare earth element record of the calcareous lacustrine sediments from a long core (SG–1) in the western Qaidam Basin, NE Tibetan Plateau. Journal of Geochemical Exploration, 145: 223–232.

Yousefi, M., 2000. Geologic Map of Eshtehard, Geological Survey of Iran, Tehran, scale 1:100000.

Zhang, J., Nancollas, G.H., 1992. Influence of calcium/sulfate molar ratio on the growth rate of calcium sulfate dihydrate at constant supersaturation. Journal of Crystal Growth, 118: 287–294.